TẠP CHÍ KHOA HỌC
TRƯỜNG ĐẠI HỌC QUY NHƠN

Từ phản ứng pha rắn trong hơi nước đến vật liệu anode hiệu năng cao cho pin lithium-ion: một khảo sát ngoại trình (ex-situ) với vật liệu lithium vanadate

Trần Hữu Hà*, Lê Thị Thanh Liễu, Huỳnh Thị Lan Phương

Khoa Khoa học Tự Nhiên, Trường Đại học Quy Nhơn, Việt Nam

Ngày nhận bài: 26/07/2025; Ngày sửa bài: 22/09/2025;
Ngày đăng bài: 06/10/2025; Ngày xuất bản: 28/02/2026

TÓM TẮT

Phản ứng pha rắn truyền thống bộc lộ nhiều nhược điểm như khó khống chế hình thái và kích thước hạt của vật liệu, tiêu hao năng lượng lớn và nhiều rủi ro môi trường. Nhằm khắc phục những vấn đề này, một kỹ thuật tổng hợp pha rắn trong điều kiện thường dưới tác động của hơi nước đã được đề xuất để tổng hợp vật liệu ứng dụng làm điện cực anode cho pin lithium-ion. Trong nghiên cứu này, lithium vanadate (Li_3VO_4) được khảo sát như một thí dụ, trong đó tính năng điện hóa của vật liệu Li_3VO_4 tổng hợp bằng phản ứng pha rắn trong hơi nước thể hiện nhiều ưu điểm vượt trội hơn vật liệu tương tự theo phương pháp truyền thống với dung lượng riêng thuận nghịch đạt 590.8 $mAh{\cdot}g^{-1}$ ở cường độ dòng riêng 100 $mA{\cdot}g^{-1}$ sau 50 chu kỳ. Các kỹ thuật ngoại trình (ex-situ), như nhiễu xạ tia X, Raman và hiển vi điện tử quét, được sử dụng nhằm làm sáng tỏ cơ chế cũng như sự biến đổi hình thái của Li_3VO_4 tổng hợp bằng phản ứng pha rắn trong hơi nước.

Từ khóa: *Pin lithium-ion, anode, phản ứng pha rắn, kỹ thuật ex-situ.*

**Tác giả liên hệ chính.*
Email: tranhuuhaqn1992@gmail.com

https://doi.org/10.52111/qnjs.2026.20105

QUY NHON UNIVERSITY
JOURNAL OF SCIENCE

From water vapor-assisted solid-state reaction to high-performance anode for lithium-ion batteries: an ex-situ investigation for a case study of lithium vanadate

Tran Huu Ha*, Le Thi Thanh Lieu, Huynh Thi Lan Phương

Faculty of Natural Science, Quy Nhon University, Vietnam

Received: 26/07/2025; Revised: 22/09/2025;
Accepted: 06/10/2025; Published: 28/02/2026

ABSTRACT

Conventional solid-state reactions (SSRs) suffer from uncontrollable morphology and particle size, massive energy consumption, and environmental risk. To address these problems, a novel approach involving ambient SSRs under water vapor has been proposed for the preparation of anode materials for lithium-ion batteries. In this work, a case study of lithium vanadate (Li_3VO_4) has been investigated in which the electrochemical properties of Li_3VO_4 from the vapor route are superior to those from conventional SSRs, delivering a reversible specific capacity of 590.8 mAh·g^{-1} at a specific current of 100 mA·g^{-1} after 50 cycles. Ex-situ techniques, such as X-ray diffraction, Raman, and scanning electron microscopy, have been employed to elucidate the mechanism of vapor-assisted SSRs in Li_3VO_4 synthesis.

Keywords: *Solid-state reaction, anode, lithium-ion batteries, ex-situ techniques.*

1. INTRODUCTION

Rising as a key component in the global race to develop electric vehicles and stationary energy storage, the advancement of lithium-ion batteries (LIBs) has been driven by the demand for high energy and power density, as well as the need for fast charging capabilities.[1] However, the preparation strategy of most active electrode materials, especially anode materials, has recently been based on conventional solid-state reactions (SSRs), which involve high energy consumption for high-temperature treatment, uncontrollable morphology, and particle size of the products due to severe aggregation. Meanwhile, wet chemistry preparations are conducted under mild conditions, but they carry the risk of releasing polluted solvents. Therefore, mimicking the solvent role of water in wet chemistry routes, a vapor-assisted SSR has been proposed to perform materials synthesis at low temperatures with controllable morphology.[2,3]

As an intercalation-type anode, lithium vanadate, Li_3VO_4, has been studied as a promising alternative to carbon-based materials due to its advantages, such as a higher theoretical capacity (591 mAh g^{-1}) and a safer operating voltage.[4] However, the application of Li_3VO_4 as an anode for LIBs is hindered by its low intrinsic electronic conductivity, which becomes more serious due to the large particle size from conventional SRR synthesis. Following a prolonged research period on these materials, various efforts, which could be divided into three categories: (i) aliovalent doping, (ii) combining

---

*Corresponding author.
Email: tranhuuhaqn1992@gmail.com

https://doi.org/10.52111/qnjs.2026.20105

with a highly conductive network or coating layer, and (iii) particle size and morphology control, have been undertaken to address this issue. For the first strategy, the aliovent such as In^{3+}/Ce^{4+},[5] Sm^{3+},[6] W^{6+},[7] Cr^{3+},[8] Cl^{-},[9] etc. Recently, the Sm has been introduced to the structure of Li_3VO_4, inducing reduction of V^{5+} to V^{4+} and oxygen vacancy, which modified the electronic band structure of the host materials toward higher electrical conductivity.[6] The conductive network and coating layer applied in Li_3VO_4-based anode include N-doped porous carbon,[10] carbon fiber,[11,12] graphene,[13] or $LiNbO_3$.[14] While the carbon-based networks provide an effective conductive pathway for electron transfer, the coating layer protects materials from side reactions with the electrolyte and minimizes solid electrolyte interphase evolution. To control the particle size and morphology of Li_3VO_4, various methods have been applied, including spray drying,[15] electrostatic spray,[16] recrystallization,[17] electrospinning,[11] etc. Among multiple strategies to address this issue, confining particle size to sub-microsize could reduce the electron transport pathway, hence improving its electrochemical performance.[2,18,19]

In this work, the vapor-assisted SSR has been utilized to prepare Li_3VO_4 as sub-micrometer spherical-like particles. The mechanism of this reaction is clarified using ex-situ techniques, which indicate the rapid phase transition of the outer layer, followed by the slow process of the completed inner reaction. The variation of morphology during the vapor-assisted SSR is also elucidated. The vapor-produced Li_3VO_4 exhibits significantly improved electrochemical performance, including a reversible capacity of 590.8 $mAh·g^{-1}$ at a specific current of 100 $mA\ g^{-1}$ after 50 cycles, which is 2.6 times higher than that of conventional SSR-Li_3VO_4.

2. EXPERIMENTALS

Chemicals: All the chemicals in this work were purchased and used without further purification. Lithium hydroxide monohydrate ($LiOH \cdot H_2O$, ≥ 98%) and vanadium pentoxide (V_2O_5 ≥ 98%) were supplied by Sigma-Aldrich, Germany. Acetylene black and anhydrous N-methylpyrrolidone (NMP, 99.5%) were sourced from Sigma-Aldrich. The electrolyte, as a 1.0 $mol·L^{-1}$ solution of lithium hexafluorophosphate ($LiPF_6$) in a 50:50 mixture of ethylene carbonate (EC) and diethyl carbonate (DEC), and poly (vinylidene fluoride) (PVDF, ≥ 99.5%) were obtained from MTI Corporation.

Materials preparation: Li_3VO_4 was prepared using both vapor-assisted SSR and conventional SSR. For vapor-assisted SSR, as shown in Scheme 1, a mixture of $LiOH·H_2O$ and V_2O_5 in a molar ratio of 3:1 was ground in a mortar. The resulting orange solids were transferred to an alumina crucible covered with aluminum foil and heated to 600 °C for 5 hours, as described by Li et al.[20] The final powder was reground and labeled as c-LVO. The precursor mixture was placed in a tea filter bag and suspended in a 20 mL vial containing 3 mL of deionized water. The sealed reactor was maintained at 80 °C for 24 hours. The resulting humid solid was dried at 80 °C for an additional 12 hours, regrinded, and labeled as v-LVO.

Materials characterization: The phase and crystal information of the as-prepared samples were investigated using X-ray diffraction (XRD) in a 2θ range of 10-80°, conducted on a Rigaku Miniflex-600 diffractometer with a Cu-Kα tube at a voltage of 40 kV and a current of 15 mA. The morphology of these samples was analyzed using field-emission scanning electron microscopy (FE-SEM), conducted on a Nova Nano SEM 450.

Ex-situ characterization: The vapor-assisted SSR was investigated at various reaction times, ranging from 30 minutes to 1, 2, 5, 12, and 24 hours. After these periods, the solid was collected and dried at 80 °C for 12 hours. The individual solids were characterized using XRD, Raman spectroscopy, and FE-SEM. The Raman spectroscopy of these v-LVOs was collected on a DXR 3xi (Thermo Fisher) under a 532-nm wavelength excitation with a laser power of 0.1 ~ 1mW, and an exposure time of 0.05 ~ 0.5s.

Electrochemical characterization: The lithium storage properties of c-LVO and v-LVO were investigated in a half-cell configuration, where a lithium metal disc served as both the reference and counter electrode. The working electrodes were fabricated using the slurry casting method. A mixture of active materials (c-LVO or v-LVO), acetylene black as a conductive agent, and PVDF as a binder, with a mass ratio of 7:2:1, respectively, was blended in NMP solvent until a uniform slurry was formed. The obtained slurry was cast on a copper foil using a doctor blade with a controlled thickness of 15 µm. The electrode was dried at 120 °C for 24 hours under vacuum, then punched into 10-mm diameter discs for further use. The CR-2032 coin cell was assembled in an Argon-Filled glovebox, with oxygen and moisture content maintained below 1.0 ppm. Typically, the half-cell was constructed from a working electrode and a lithium metal foil, separated by a glass microfiber separator soaked in the electrolyte. The newly assembled coin-cells were rested for 12 hours before further experiments.

The galvanostatic properties of the half-cells were performed on the NAGANO-BTS-4000H battery station in a potential range of 0.10–3.00 V (vs. Li/Li$^+$) at a specific current of 100 mAh·g^{-1}. The electrochemical behavior of lithium storage in these cells was clarified using cyclic voltammetry (CV) over the relevant potential range at a scan rate of 0.05 mV·s^{-1}. The electrochemical impedance spectroscopy (EIS) results were obtained in a frequency range of 0.01 – 10^5 Hz under an ab alternative current amplitude of 5 mV. The CV and the EIS results were recorded on the MultiAutolab/M101 system.

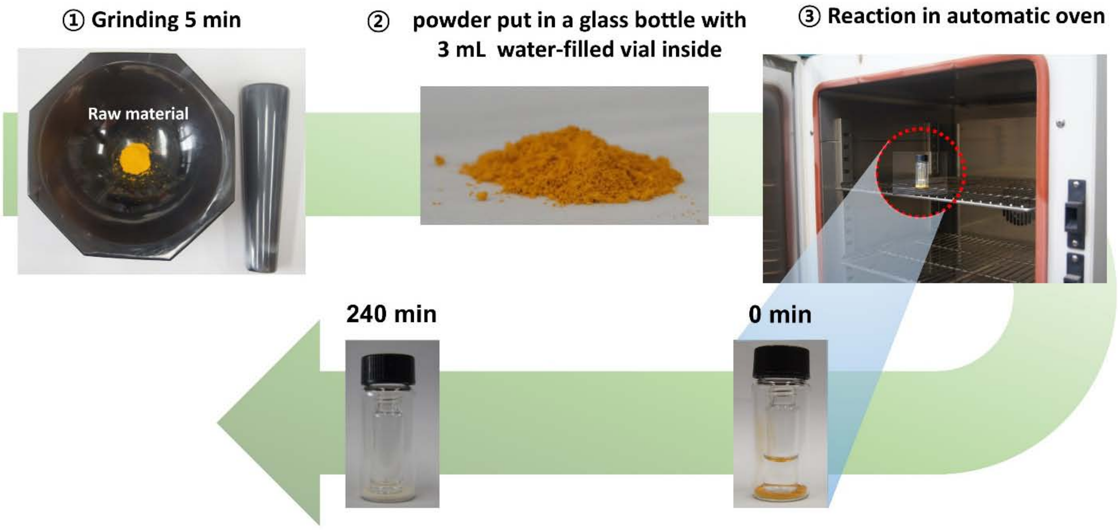

Scheme 1. Illustration of vapor-assisted solid-state reaction for v-LVO preparation.

3. RESULTS AND DISCUSSION

Crystal structure analysis: The XRD patterns of the as-prepared c-LVO and v-LVO are exhibited in Figure 1a. Accordingly, the XRD pattern of c-LVO comprises the signals at 2θ of 16.3°, 21.5°, 22.8°, 21.3°, 28.1°, 32.7°, 35.9°, 36.3°, 50.2°, 58.6°, 66.2°, and 70.8° corresponding to the (100), (110), (011), (111), (200), (002), (201), (202), (320), (203), and (322). Similarly, the observations from the XRD diffraction of v-LVO are almost the same as those of c-LVO, demonstrating that the sample

https://doi.org/10.52111/qnjs.2026.20105

prepared via vapor-assisted SSR is crystallized in the orthorhombic phase. The illustration of the crystal structure of orthorhombic Li_3VO_4 is presented in Figure 1b. Therein, the lattice units of Li_3VO_4 are constructed from tetrahedra of LiO_4 and VO_4 connecting via oxygen atoms. However, the diffraction of the v-LVO is broadening compared to that of the c-LVO. As shown in the insets of Figure 1a, the full width at half maximum (FWHM, β) of the (111) peak in v-LVO is larger than that of c-LVO, demonstrating lower crystallinity and smaller crystallite size. To calculate the crystallite size, the Williamson-Hall (WH) approach was employed. According to Figure 1c and Table 1, the plots of (βcosθ) vs (4sinθ) of the c-LVO and v-LVO indicate the intercepts of 0.046 and 0.0.320, corresponding to crystallite sizes of 31.2 nm and 4.5 nm, respectively. In addition, the microstrain in the lattice structures of these samples is also derived from the slope of the WH plot. Therein, the higher slope of c-LVO induces a larger value of microstrain of 145, 2.8 times higher than that of the v-LVO. The crystal structure analysis indicates that vapor-assisted SSRs conducted in ambient conditions can produce more polyscrystalite properties with lower lattice strain, which is favorable for lithium transport during lithiation/delithiation.

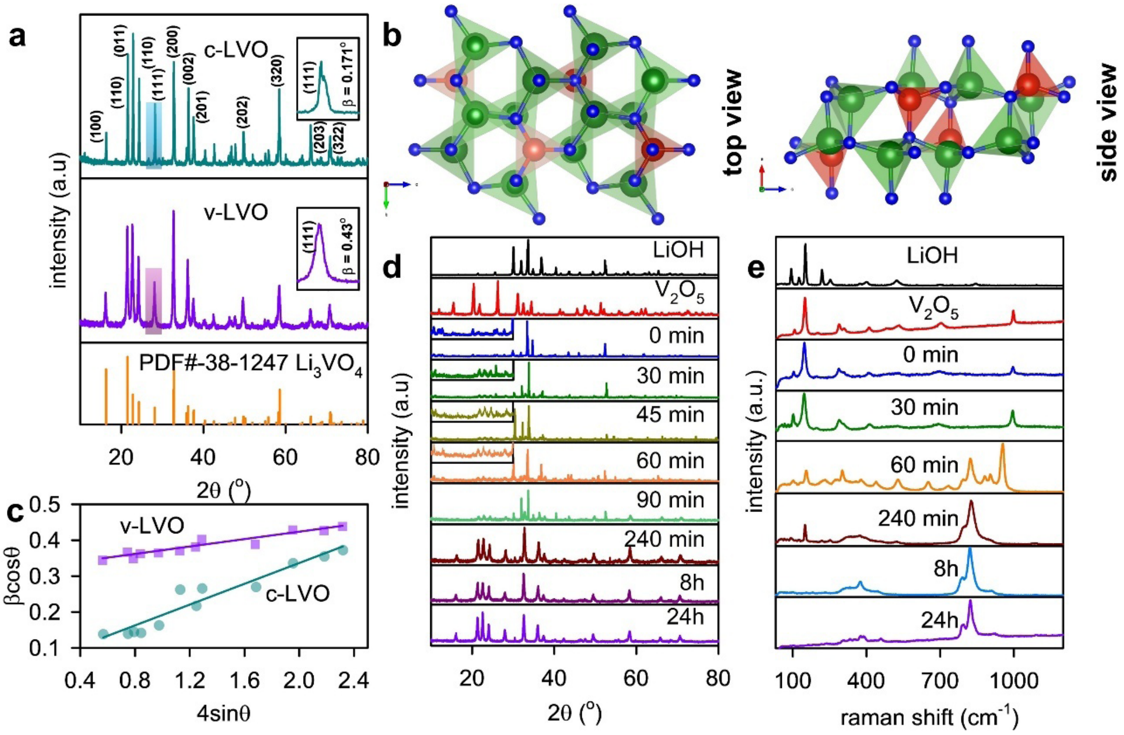

Figure 1. (a) XRD patterns of the c-LVO and v-LVO (the insets are the enlargement of XRD patterns in 2θ-range of 31-34°; (b) the illustration of top and side views of orthorhombic Li_3VO_4, where red, green, and blue represent vanadium, lithium, and oxygen; (c) Williamson-Hall plots of c-LVO and v-LVO; (d) ex-situ XRD and (e) ex-situ Raman spectroscopy of the LiOH, V_2O_5, and v-LVO after various reaction times from 0 min to 24 hours.

Table 1. Results derived from WH method for determining crytallite size and microstrain of c-LVO and v-LVO.

Sample	WH equation βcosθ = 4εsinθ + Kλ/D	Intercept (Kλ/D)	Crystallite size (nm)	Slope (ε)	Microstrain ($\times 10^{-3}$)
c-LVO	y = 0.14498x + 0.04643	0.04643	31.190	0.14498	144.98
v-LVO	y = 0.05167x + 0.32032	0.32032	4.521	0.05167	51.67

Ex-situ investigation on vapor-assisted SSR The formation of the v-LVO was investigated using ex-situ XRD. According to Figure 1d, the diffractions of the $LiOH·H_2O$ including peaks at 2θ = 30.1, 31.1, 32.9, 34.9, 36.8, 40.3, and 52.5°, corresponding to the (-111), (-201), (220), (130), (021), (-311), and (400) planes of momoclinic structure with a space group of C2/m ascribing to PDF#01-076-1073. Meanwhile, the XRD pattern of V_2O_5 comprises signals at 2θ = 15.4, 20.3, 21.8, 26.4, 31.2, 32.4, 34.5, 41.4, 47.6, and 51.2° matching to the (200), (001), (101), (110), (400), (011), (002), (600), and (020) plane of the orthorhombic lattice of α-V_2O_5 ($P2_1/m$) according to PDF#41-1426. Those lattice diffractions are well-observed in the mixing solid's XRD pattern (0 min). After being exposed to water vapor for 30 minutes, the XRD pattern exhibits significant variation in the 2θ range of 20-30°, indicating the formation of a newly formed Li_3VO_4 phase at the interface of the precursors. However, this variation remains for the next two hours, as illustrated by the insignificant changes in the XRD patterns at 45, 60, and 90 minutes of reaction. After 240 minutes of reaction, the evolution of Li_3VO_4 is observable, while the precursor is indicated as an impurity with low content. After 8 hours of reaction, no impurity could be observed, indicating the complete reaction.

A similar phenomenon can be inferred from the ex-situ Raman data, as shown in Figure 1d. As shown in the Raman spectrum of LiOH, the strong peaks in the range of 60 – 300 cm^{-1} are assigned to the ionic bonds of Li^+ and OH^-, while the low-intensity bands at 401 and 533 cm^{-1} are ascribed to the libration motion of water molecules.[21] The V_2O_5 Raman spectrum comprises the stretching modes of V=O located at 991.3 cm^{-1}, the vibration of bridging V-O-V at 702.5 cm^{-1}, the stretching motion of ladder V-O at 528.3 cm^{-1}, the in and out-of-phase oscillation of V and O atoms at 292.1 and 282.4 cm^{-1}, while the shearing distortion of these atoms is attributed to the lowest Raman shift bands at 201.1 and 147.5 cm^{-1}.[22] Those signals of vanadium oxides are clearly observed in mixing precursors, while the LiOH-related peak is missing, which could be attributed to the high dissolution of LiOH. As shown in the Raman spectrum of the reaction mixture after 30 minutes, there is no significant variation compared to the original mixture, indicating a low product content and a slow reaction rate for the solid-state reaction. After 60 minutes of reaction, the Raman spectrum exhibits various new bands related to the interaction of LiOH and V_2O_5. Therein, the vanishment of the 991.3 cm^{-1} peak along with the addition of new peaks at 966.1 and 946.2 cm^{-1} corresponding to the phase transition of α-V_2O_5 to γ-$Li_xV_2O_5$,[22,23] which could be formed by the intercalation of lithium-ion into the layered structure of V_2O_5. Additionally, the newly emerging signals appeared at 830.1 and 780.4 cm^{-1}, assigned to the symmetric and asymmetric stretching vibrations of VO_4^{3-} units, indicating the formation of Li_3VO_4. The vibration of VO_4^{3-} is also characterized by a band around 400 cm^{-1}, as reported in previous studies.[14,24] However, the remaining signals below 200 cm^{-1} until 240 min demonstrate a slow rate and incomplete reaction. For a longer reaction time, the Raman spectra consist of only two bands at 300–450 cm^{-1} and 700–850 cm^{-1}, characteristic of orthorhombic Li_3VO_4, which confirms the pure phase of the products and is in good agreement with XRD data.

The morphology evolution of Li_3VO_4 prepared via vapor-assisted SSR is investigated using the FE-SEM technique. As shown in Figures 2a,b, the raw V_2O_5 exhibits polyhedrons of a few hundred micrometers, while the LiOH is observed as an aggregation of particles of a few tens of nanometers. After the precursors are mixed (Figure 2c), the surface of V_2O_5 polyhedrons is covered with LiOH nanoparticles, which could be explained due to (i) the different solubility of precursors: LiOH is hydrophilic and highly dissolved in water, but V_2O_5 is hydrophobic and performs low solubility, (ii) acid – base nature of precursors: LiOH is a strong base and V_2O_5 is

https://doi.org/10.52111/qnjs.2026.20105

acidic surface, hence, under a vapor surrounding, LiOH tends to absorb water and etching to V_2O_5 surface by acid-base reaction. The etching behavior of LiOH is enlarged by the time of reaction, as shown in Figure 2d, and fully covers the polyhedrons. After 60 minutes of reaction, the coverage layer of the product tends to form as long streptococci-like particles (Figure 2e). These particles become larger and break down into nanorods after 120 minutes (Figure 2f). Due to the high solubility of Li_3VO_4, the newly formed product continues to be etched by water vapor. According to Figures 2g,h, after longer reaction times, the long strings break into shorter rods, accumulate on a porous surface, and form aggregated spherical particles. The morphology evolution of Li_3VO_4 is illustrated in Figure 2i. Compared to the v-LVO, the Li_3VO_4 particles synthesized by the conventional SSR have a larger size, reaching a few micrometers. The smaller size of v-LVO is preferable for improving electrochemical performance in lithium-ion storage due to shortening the electron and ion diffusion pathways, enhancing electrolyte/electrode contact, and alleviating lattice strain and stress caused by volume variation during lithiation/delithiation. Therefore, it is promising that the v-LVO could provide better electrode cycling performance compared to that of the c-LVO, as demonstrated in the following section.

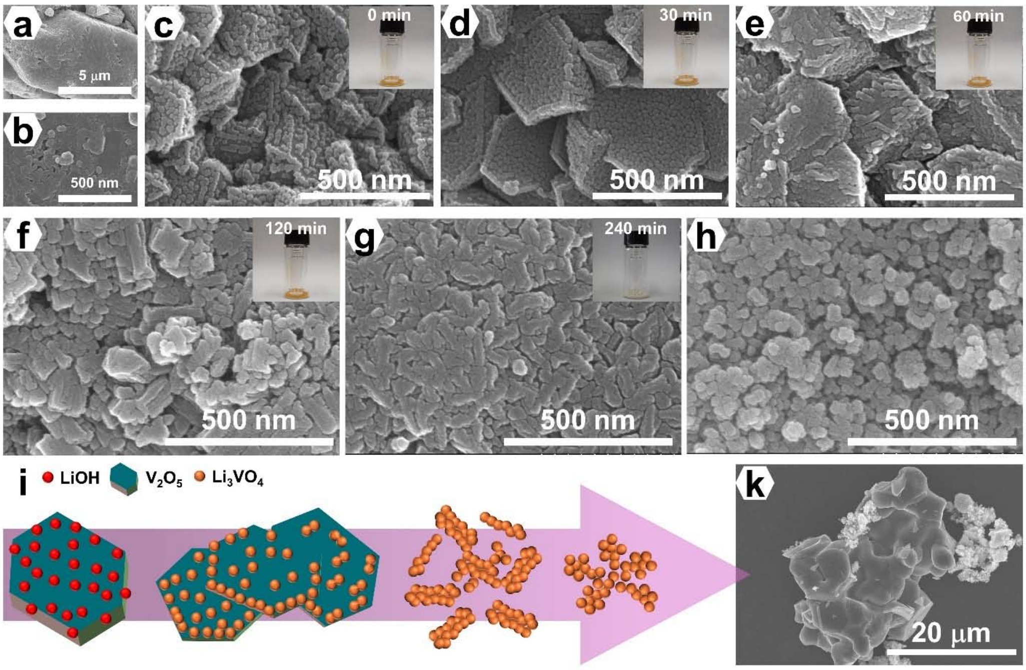

Figure 2. Morphology evolution of Li_3VO_4 synthesized via vapor-assisted solid-state reaction: FE-SEM images of (a) V_2O_5; (b) $LiOH{\cdot}H_2O$, (c) precursors after mixing (0 mins); and solids obtained after relevant reaction times of (d) 30 mins; (e) 60 mins; (f) 120 mins; (g) 240 mins; (h) 24 hours; (i) illutration of morphology evolution of Li_3VO_4 prepared via vapor-assisted solid-state reaction; (k) FE-SEM image of c-LVO.

Electrochemical performance: The lithium-ion storage mechanism of the obtained materials is studied using the CV curves, as shown in Figures 3a,b. As shown in Figure 3b, the first cathodic curve of the v-LVO exhibits two peaks at 0.76 and 0.51 V (vs. Li/Li^+). These peaks are attributed to the intercalation of lithium ions into Li_3VO_4, resulting in $Li_{3+x}VO_4$, which is associated with the reduction of V^{5+} to V^{4+} and V^{3+}.[25] The correlative behavior is also observed in the c-LVO with a signal at 0.72 V (vs. Li/Li^+) and a shoulder below 0.5 V (vs. Li/Li^+) (Figure 3a). The lower-potential peaks in both electrodes tend to broaden, which can be attributed to the formation of a solid electrolyte interface (SEI) layer resulting from the decomposition of electrolyte salts and solvents. In the anodic process, the v-LVO electrode exhibits a shoulder signal comprising a lower-intensity peak at 1.15 V (vs. Li/Li$^+$) and a stronger peak at 1.31 V (vs. Li/Li$^+$), corresponding to the reversible delithiation from $Li_{3+x}VO_4$. Compared to c-LVO, the potential gap of the redox peaks related to the insertion and extraction of lithium ions in v-LVO is narrower (the inset of Figures 3a,b), indicating less polarization impedance of this electrode. This can be attributed to the nanosized particles of v-LVO compared to the microsize of c-LVO, which may accelerate lithium and electron transport, thereby improving the kinetics of the electrode reaction.[25-27] In the subsequent cycles, the reduction peaks shift to higher potentials, while the oxidation signals shift to lower potentials, indicating a further decrease in potential differences. Therein, the redox peak shift in v-LVO is more than what is observed in the c-LVO, resulting in a smaller gap of 0.22 V compared to 0.33 V, respectively. In addition, the fact that the CV curve forms a larger area, and the redox peaks are sharper for v-LVO, could demonstrate an improved kinetic behavior of this electrode, promising better electrochemical performance.[28,29]

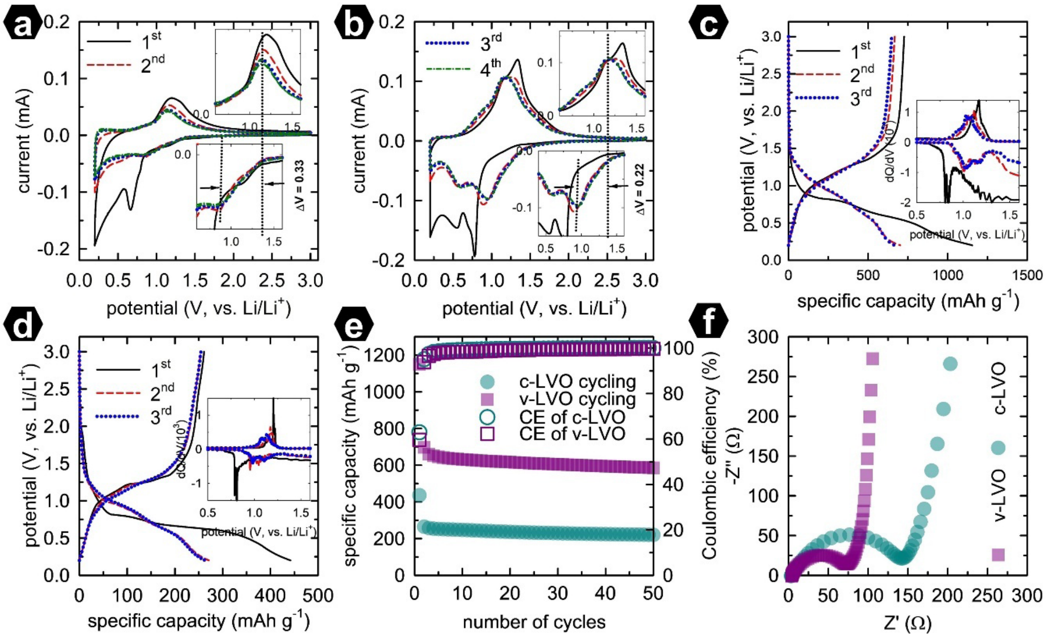

Figure 3. CV curves of the first four cycles of (a) c-LVO and (b) v-LVO electrodes, the insets are the enlargement of relevant data in the selected potential ranges; galvanostatic charge-discharge profile of the first three cycles of (c) v-LVO and (d) c-LVO, the insets are the dQ/dV plots of relevant data in the selected potential ranges; (e) cycling performance and Coulombic efficiency of the c-LVO and v-LVO electrodes; and the Nyquist plots of c-LVO and v-LVO electrodes. All of the experiments are conducted in the potential range of 0.2 – 3.0 V vs. Li/Li$^+$, and at a scan rate of 0.5 mV·s^{-1} for CV and at a specific current of 100 mA·g^{-1} for cycling.

The galvanostatic charge-discharge profiles of the v-LVO and c-LVO electrodes are illustrated in Figures 3c and 3d. The initial discharge process can be categorized into three distinct regions: (i) a potential drop above 1.0 V (vs. Li/Li$^+$); (ii) two continuous plateaus around the potentials of 0.75 V and 0.60 V (vs. Li/Li$^+$); and (iii) a subsequent decline towards the low cut-off potential. The first plateau corresponds to the reduction of V^{5+} to V^{4+}, while the following plateau is associated with the further reduction to V^{3+}, consistent with the results from CV. In the charge profile and subsequent cycles, the reversible plateaus are less discernible, which may be due to the nanosize effect that minimizes the potential gap between the two-phase transitions.[30,31] However, as indicated in the inset, the dQ/dV plots effectively highlight these transition steps. The v-LVO electrode achieves a specific discharge capacity of 1153.9 mAh·g^{-1}

and a specific charge capacity of 726.4 mAh·g^{-1}, yielding a Coulombic efficiency (CE) of 62.8%. In comparison, the first specific discharge and charge capacities for the c-LVO electrode are 441.8 mAh·g-1 and 263.5 mAh·g^{-1}, respectively, resulting in a first CE of 59.6%. The relatively low CE observed in both electrodes can be attributed to the irreversible formation of the SEI layer. The lower CE of the c-LVO electrode is linked to its diminished kinetic characteristics, which contribute to a thicker SEI layer. In contrast, the v-LVO electrode demonstrates a higher specific capacity of 590.8 mAh·g^{-1} - 2.6 times greater than that of the c-LVO electrode - and retains 81.3% of its capacity after 50 cycles. The impedance behavior of these electrodes was investigated using EIS techniques, and the obtained Nyquist plots are shown in Figure 3f. Accordingly, the Nyquist plots perform a semi-circle characterized by the charge transport resistance, and a linear tail indicating diffusion properties. As shown in Figure 3f, the v-LVO electrode exhibits a semicircle with a smaller diameter, indicating improved charge transfer kinetics compared with the c-LVO electrode. This observation is correlated to the reduction in particle size, resulting in enhanced electrical contact and shortening the charge transport pathway, as mentioned above. The recent results of v-LVO are comparable with other publications, as shown in Table 2. The enhanced electrochemical performance of the v-LVO can be ascribed to improved kinetic properties resulting from the nanosize control achieved through the vapor-assisted SSR method.

Table 2. A comparison of the electrochemical performance of Li_3VO_4 nanorod-carbon composite and other related anode materials. (LVO = Li_3VO_4)

Materials	Synthesis method	Operating potential window (V, vs. Li/Li$^+$)	Specific current (mA·g^{-1})	Specific capacity (mAh·g^{-1}) – cycle	Retention (%)	Ref.
LVO/rGO	solvothermal	0 – 3.0	150	410.7 – 200	69.3	[32]
Facet-controlled LVO	Rapid hydrothermal	0.2 – 3.0	25	315.0 – 50	-	[33]
LVO@C	Freeze drying, sintering and water etching	0.01 – 3.0	200	850.8 – 150	-	[34]
LVO@C	Sol-gel method	0.2 – 3.0	100	299.0 – 100	99	[35]
W^{6+}-doped LVO	Spray-drying and sintering	0.2 – 3.0	40	305.8 – 200	91.4	[7]
Sm-doped LVO/C	Sol-gel and carbonization	0.2 – 3.0	100	379.5 – 50	93.7	[6, 36]
Ge-doped γ-LVO	Calcination	0.2 – 3.0	2000	383.0 – 1500	111.5	[36]
1D-LVO/Carbon fiber	Chemical vapor deposition	0 – 3.0	200	516.2 – 100	-	[12]
$LiNbO_3$-coated LVO	Sol-gel and calcination	0.05 – 2.5	40	481.0 – 100	90	[14]
LVO mesocube	Solid-state reaction and hydrothermal	0.02 – 3.0	200	262.6 – 500	97.5	[17]
LVO@C	Calcination	0.01 – 3.0	150	855.0 – 300	-	[37]
LVO nanoparticles	Vapor-assisted solid-state reaction	0.2 – 3.0	100	590.8 – 50	81.3%	**This work**

4. CONCLUSIONS

In this work, Li_3VO_4 is prepared using both conventional and vapor-assisted SSR methods. A comparative study has been conducted to demonstrate the ability of the vapor-assisted SSR in the synthesis of pure-phase Li_3VO_4 under ambient conditions. The phase transformation of Li_3VO_4 during vapor-assisted SSR progression has been investigated using ex-situ XRD and Raman spectroscopy, demonstrating that the product phase appears at a slow reaction rate at the beginning of the procedure, and the reaction does not complete until at least 240 minutes. Meanwhile, the morphological evolution of Li_3VO_4 throughout vapor-assisted SSR has been monitored using the FE-SEM technique, elucidating the slow etching of LiOH over the V_2O_5 surface, from polyhedrons to long strings, until the accumulation of nanospheres. The enhanced electrochemical properties of vapor-prepared materials are attributed to the nanosize effect, which is beneficial for both lithium-ion and electron transport, thereby accelerating the kinetics of electrode reactions.

Acknowledgment

This research is conducted within the framework of science and technology projects at the institutional level of Quy Nhon University under the project code T2025.886.06.

REFERENCES

1. C. Xu, Q. Dai, L. Gaines, M. Hu, A. Tukker, B. Steubing. Future material demand for automotive lithium-based batteries, *Communications Materials,* **2020**, *1*(1), 99.
2. H. T. Huu, N. H. Vu, H. Ha, J. Moon, H. Y. Kim, W. B. Im. Sub-micro droplet reactors for green synthesis of Li_3VO_4 anode materials in lithium-ion batteries, *Nature Communications*, **2021**, *12*(1), 3081.
3. Y. Shibuta, T. Hasegawa, S. W. Kim, K. Uematsu, K. Toda, M. Sato. Mild condition synthesis without high temperature process of Eu^{2+}-doped barium orthosilicate nanophosphor via Water-Assisted Solid-State Reaction (WASSR) method, *Journal of Alloys and Compounds*, **2019**, *788*, 1009–1012.
4. X. Ye, Y. Fan, Q. Tong, Z. Chen, M. Zhu, J. Huang, X. Ding. Review of Li_3VO_4 anode materials for energy storage, *Critical Reviews in Solid State and Materials Sciences*, **2023**, *48*(6), 754–774.
5. Y. Wan, Z. Chang, X. Xie, J. Li, S. Chai, S. Zhou, Q. He, C. Fu, M. Feng, G. Cao. In/Ce co-doped Li_3VO_4 and nitrogen-modified carbon nanofiber composites as advanced anode materials for lithium-ion batteries, *ACS Applied Materials & Interfaces*, **2022**, *14*(47), 52702–52714.
6. Y. Wan, X. Xie, S. Zhou, W. Li, J. Ma, Y. Zhou, Y. Song, J. Zhou, A. Pan. Sm doping-enhanced Li_3VO_4/C electrode kinetics for high-performance lithium-ion batteries, *ACS Applied Energy Materials*, **2025**, *8*(6), 3581–3591.
7. Y. S. Hsiao, J. H. Huang, L. Y. Weng, T. H. Cheng, H. H. Chiang, C. Z. Lu, H. C. Weng, L. Thomsen, B. Cowie, W. K. Pang. Advancing Li_3VO_4 as a high-performance anode material for use in lithium-ion batteries and lithium-ion capacitors, *Chemical Engineering Journal*, **2024**, *489*, 150973.
8. C. C. Lu, H. F. Lin, J. H. Huang, Y. C. Yen, W. K. Pang, H. C. Weng, S. C. Hsu, Z. L. Tseng. Cr-doped and carbon-coated Li_3VO_4 derived from a metal–organic framework for high-performance anode applications, *Journal of Energy Storage*, **2025**, *136*, 118390.
9. Z. Zhang, J. Xu, D. Zhang, H. Ma, T. Li, T. Xiao, C. Pei, S. Ni. Concise strategies to enhance the high-rate performance of Li_3VO_4 anodes: Cl doping, carbon coating, and spherical architecture design, *Transactions of Tianjin University*, **2023**, *29*(2), 110–119.
10. S. Yang, C. Pei, D. Zhang, B. Sun, P. Li, T. Li, S. Ni. Hierarchical porous N-doped carbon nanofibers with encapsulated Li_3VO_4 nanoparticles for lithium-ion storage, *ACS Applied Nano Materials*, **2024**, *7*(1), 827–835.
11. J. Yao, X. Bai, D. Zhang, S. Yang, C. Pei, S. Ni. Fast kinetics for lithium storage rendered by Li_3VO_4 nanoparticles/porous N-doped carbon

https://doi.org/10.52111/qnjs.2026.20105

nanofibers, *Journal of Energy Storage*, **2024**, *102*, 114193.

12. J. Song, A. Y. Maulana, W. Jae, H. Gim, B. Yun, C. M. Futalan, J. Kim. One-dimensional Li_3VO_4/carbon fiber composites for enhanced electrochemical performance as an anode material for lithium-ion batteries, *Journal of Materials Science & Technology*, **2023**, *140*, 142–152.
13. C. Yang, T. Long, R. Li, C. Wu, Y. L. Ding. Pseudocapacitance dominated Li_3VO_4 encapsulated in N-doped graphene via 2D nanospace confined synthesis for superior lithium-ion capacitors, *Chinese Chemical Letters*, **2025**, *36*(2), 109675.
14. E. Elmaataouy, A. Chari, A. A. Shami, G. Elomari, M. Aqil, J. Gim, R. Amine, H. Martinez, J. Alami, O. Mounkachi. Improved cycle stability and high-rate capability of $LiNbO_3$-coated Li_3VO_4 as anode material for lithium-ion battery, *Journal of Energy Storage*, **2024**, *86*, 111351.
15. K. Matsumura, Y. Hikichi, D. Saito, E. Iwama, W. Naoi, P. Rozier, P. Simon, K. Naoi. Cation-disordered structure in Li_3VO_4 anodes achieved via simple spray-drying for unprecedented rate capability, *ACS Energy Letters*, **2025**, *10*(5), 2184-2192.
16. L. Kuang, B. Sun, S. Yang, D. Zhang, C. Pei, P. Li, T. Xiao, S. Ni. Prominent long-life and high-rate performance rendered by crystallized Li_3VO_4 embedded in amorphous carbon nanoflakes, *Journal of Materials Chemistry A*, **2024**, *12*(7), 4008-4018.
17. D. Wang, Y. Zhao, P. Liu, C. Li, C. Yang, Y. Sun, M. Zhang, Y. Yang, Q. Wang, G. Dai. Li_3VO_4 mesocubes with exposed (200) facet as dendrite-free anode materials for high-safety Li-ion batteries, *Chemical Engineering Journal*, **2024**, *502*, 157805.
18. J. Liu, P. J. Lu, S. Liang, W. Wang, M. Lei, S. Tang, Q. Yang. Ultrathin Li_3VO_4 nanoribbon/graphene sandwich-like nanostructures with ultrahigh lithium-ion storage properties, *Nano Energy*, **2015**, *12*, 709-724.
19. G. Shao, L. Gan, Y. Ma, H. Li, T. Zhai. Enhancing the performance of Li_3VO_4 by combining nanotechnology and surface carbon coating for lithium-ion batteries, *Journal of Materials Chemistry A*, **2015**, *3*(21), 11253-11260.
20. H. Li, X. Liu, T. Zhai, D. Li, H. Zhou. Li_3VO_4: a promising insertion anode material for lithium-ion batteries, *Advanced Energy Materials*, **2013**, *3*(4), 428–432.
21. V. Tyutyunnik. Lithium hydroxide monohydrate single crystals: infrared reflectivity and Raman study, *Journal of Raman Spectroscopy*, **2000**, *31*(7), 559-563.
22. P. Shvets, O. Dikaya, K. Maksimova, A. Goikhman. A review of Raman spectroscopy of vanadium oxides, *Journal of Raman Spectroscopy*, **2019**, *50*(8), 1226-1244.
23. H. Jung, K. Gerasopoulos, A. A. Talin, R. Ghodssi. A platform for *in situ* Raman and stress characterizations of V_2O_5 cathode using MEMS device, *Electrochimica Acta*, **2017**, *242*, 227–239.
24. G. Yang, B. Zhang, J. Feng, Y. Lu, Z. Wang, V. Aravindan, M. Aravind, J. Liu, M. Srinivasan, Z. Shen. Morphology controlled lithium storage in Li_3VO_4 anodes, *Journal of Materials Chemistry A*, **2018**, *6*(2), 456-463.
25. C. Mu, K. Lei, H. Li, F. Li, J. Chen. Enhanced conductivity and structure stability of Ti^{4+} doped Li_3VO_4 as anodes for lithium-ion batteries, *The Journal of Physical Chemistry C*, **2017**, *121*(47), 26196-26201.
26. Y. Wei, C. W. Ryu, K. B. Kim. Improvement in electrochemical performance of V_2O_5 by Cu doping, *Journal of Power Sources*, **2007**, *165*(1), 386-392.
27. K. Wang, H. Fu, Z. Li, M. Xia, X. Liang, R. Qi, G. Cao, X. Lu. Enhancing the rate performance of a Li_3VO_4 anode through Cu doping, *ChemElectroChem*, **2018**, *5*(3), 478-482.
28. J. Zhou, B. Zhao, J. Song, B. Chen, X. Ma, J. Dai, X. Zhu, Y. Sun. Optimization of rate capability and cyclability performance in Li_3VO_4 anode material through Ca doping, *Chemistry - A European Journal*, **2017**, *23*(64), 16338-16345.

29. Z. Li, J. Li, Y. Zhao, K. Yang, F. Gao, X. Li. Structure and electrochemical properties of Sm-doped $Li_4Ti_5O_{12}$ as anode material for lithium-ion batteries, *RSC Advances*, **2016**, *6*(19), 15492–15500.

30. Y. Liu, W. Wang, H. Huang, L. Gu, Y. Wang, X. Peng. The highly enhanced performance of lamellar WS_2 nanosheet electrodes upon intercalation of single-walled carbon nanotubes for supercapacitors and lithium-ion batteries, *Chemical Communications*, **2014**, *50*(34), 4485–4488.

31. H. T. Huu, H. T. Le, V. P. Nguyen, T. T. H. Nguyen, T. X. D. Nguyen, V. T. Nguyen, S.-J. Kim, V. Vo. Facile one-step synthesis of g–C_3N_4–supported WS_2 with enhanced lithium storage properties, *Electrochimica Acta*, **2020**, *341*, 136010.

32. J. Cao, D. Zhang, P. Sun, D. Yang, S. Ni. Low temperature and atmospheric pressure fabrication of Li_3VO_4/rGO hybrid as high-performance anode for lithium-ion batteries, *Ionics*, **2021**, *27*(3), 1041-1048.

33. Y. Shi, Y. Zhang, L. Liu, Z. Zhang, J. Wang, S. Chou, J. Gao, H. D. Abruña, H. Li, H. Liu. Rapid hydrothermal synthesis of Li_3VO_4 with different favored facets, *Journal of Solid State Electrochemistry*, **2017**, *21*(9), 2547-2553.

34. J. Xu, P. Liang, D. Zhang, C. Pei, Z. Zhang, S. Yang, S. Ni. A reverse-design-strategy for C@ Li_3VO_4 nanoflakes toward superb high-rate Li-ion storage, *Journal of Materials Chemistry A*, **2021**, *9*(32), 17270–17280.

35. E. Thauer, G. Zakharova, S. Wegener, Q. Zhu, R. Klingeler. Sol-gel synthesis of Li_3VO_4/C composites as anode materials for lithium-ion batteries, *Journal of Alloys and Compounds*, **2021**, *853*, 157364.

36. J. Deng, C. Lv, T. Jiang, S. Ma, X. Liu, C. Lin. Selective doping to controllably tailor maximum unit-cell-volume change of intercalating Li^+-storage materials: a case study of γ phase Li_3VO_4, *Advanced Science*, **2022**, *9*(24), 2106003.

37. P. Li, C. Zhu, X. Chen, M. He, B. Sun, C. Pei, D. Zhang, S. Ni. Self-adaptive built-in electric fields drive high-rate lithium-ion storage in C@ Li_3VO_4 heterostructures, *Advanced Functional Materials*, **2025**, 2503584.

https://doi.org/10.52111/qnjs.2026.20105